Simulation of an Extratropical Cyclone in the Southern Hemisphere: Model Sensitivity

I. ORLANSKI, J. KATZFEY, C. MENENDEZ,* AND M. MARINO*

Geophysical Fluid Dynamics Laboratory/NOAA, Princeton University, Princeton, New Jersey
**Centro de Investigaciones para la Dinamica del Mar y la Atmosfera, CIMA/CONICET, Buenos Aires, Argentina*

(Manuscript received 9 April 1990, in final form 27 December 1990)

ABSTRACT

A rapidly deepening cyclone that occurred over the South Pacific on 5 September 1987 was investigated in order to assess the possible factors contributing to its development. Cyclogenesis took place when a disturbance in the subtropics merged with a wave in the polar westerlies. Analysis revealed that the evolution of the cyclone system was associated with the interaction of a potential vorticity anomaly from the subpolar region with a subtropical surface disturbance in a manner typical of "Class B" cyclogenesis. As the storm intensified, the subtropical jet merged with the polar jet, producing a strong poleward heat transport characteristic of baroclinic systems. However, the absence of tilt to the frontal zone, together with weak vertical wind shear, was suggestive of a significant barotropic component to the storm. The zonal average of potential vorticity over the storm displayed large regions where the meridional gradients have different signs, indicating that the system could have developed initially by internal instabilities (barotropic and/or baroclinic) without significant external forcings.

Sensitivity experiments were conducted to determine the role of surface processes in the development of the storm. It was found that development was insensitive to both surface heat fluxes and the presence of South American topography, with little change in either the circulation or kinetic energy of the storm. Intensification of the storm was substantially affected by surface frictional effects, as indicated by significant increases in the vertically averaged kinetic energy when the surface roughness was reduced. The results suggest a need to reduce the roughness heights not only over sea ice, but over the ocean in areas of strong winds as well.

1. Introduction

Although many possible mechanisms have been postulated to explain the rapid development of extratropical cyclones, the causes are still not fully understood, especially in the Southern Hemisphere where fewer storms have been studied. Previous studies of the Southern Hemisphere circulation (van Loon and Jenne 1972; Streten 1980; Carleton 1981) hypothesized that the spatial and temporal variability of cyclogenesis is related to the semiannual oscillation of the circumpolar vortex, the location of the Oceanic Polar Front, and the position of the Antarctic ice pack. The locations of cyclones by seasons have been determined through studies of cloud vortices in satellite images (Carleton 1979, 1981). Four principal regions of winter cyclone frequency can be seen in Fig. 1, along with their relation to surface features in the Southern Hemisphere. The four high-frequency areas are in the South Atlantic, the south Indian, and the western and eastern South Pacific oceans. A close correspondence between the bands of maximum vortex frequencies with both the oceanic polar front and the Antarctic pack ice boundaries is also apparent (see Fig. 1). Although cyclonic activity is prevalent all year in the middle to high latitudes of the Southern Hemisphere (Streten and Troup 1973; Carleton 1979, 1981; Physick 1981), the frequencies of winter cyclones are more than double those of the summer cyclones. These variations in space and time suggest a diversity of triggering mechanisms for cyclogenesis.

With increased satellite coverage and availability of daily archived global data from weather prediction models at the world meteorological centers, a more coherent picture of Southern Hemispheric climatology has developed (Trenberth 1981; Oort 1983; Karoly and Oort 1987; Randel 1988). A dual jet structure of the westerlies has been found for a large part of the Southern Hemisphere, which provides an additional energy source for the development of eddies. Trenberth (1986) has shown that some wave development over the western Pacific may be due to barotropic processes, particularly over eastern Australia where frequent blocking events occur. He suggested that the dual jet structure could be barotropically unstable and may be the origin of some of the eddy activity in the western South Pacific.

The region west of South America (the location of the storm analyzed in this paper) also experiences high cyclone frequency, shaping both the daily weather of

Corresponding author address: Isidoro Orlanski, Geophysical Fluid Dynamics Laboratory/NOAA, P.O. Box 308, Princeton University, Princeton, NJ 08542.

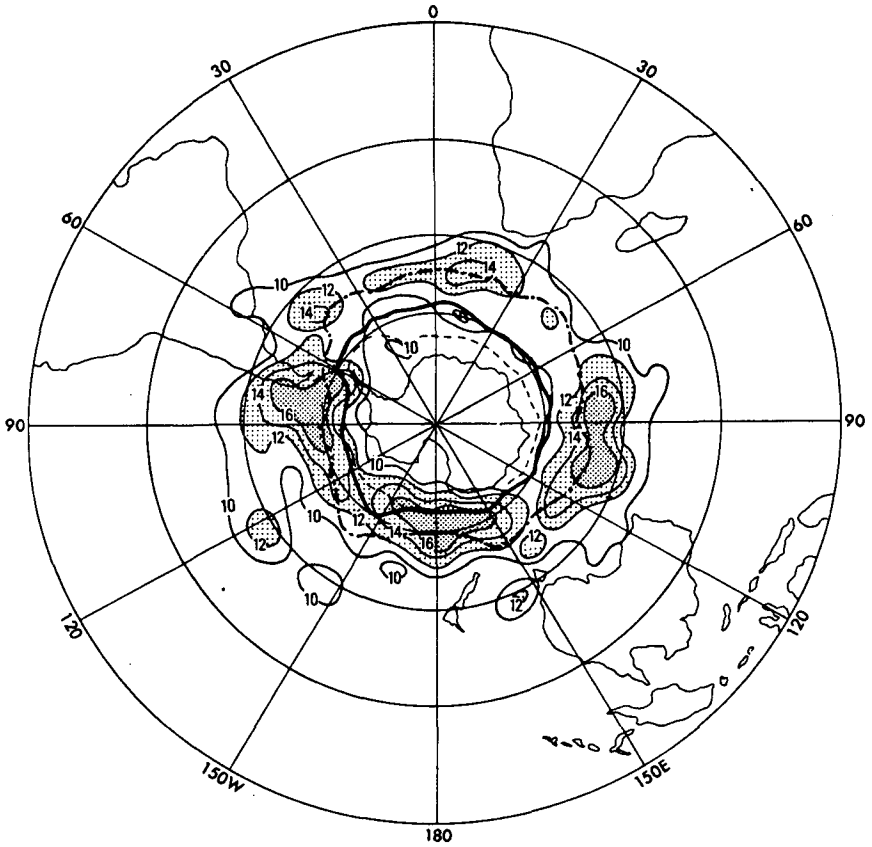

FIG. 1. Relationship of cyclone frequency with the Oceanic Polar Front and pack ice boundaries. Contours are mean monthly normalized vortex frequencies in each 5° latitude by 10° longitude unit for June through September of 1973–77, light shading above 12 and heavy shading above 16. The Oceanic Polar Front is indicated by one dot-dashed line; the September ice margin by the moderate solid line, and the June pack ice limit by the light dashed line.

South America and the planetary flow. Typically, depressions move eastward into the region and intensify. As they mature, these cyclones become nearly stationary and remain in the same geographical region for several days before migrating eastward as they dissipate. Possible factors for enhanced cyclogenesis in this region include: 1) the large gradient of sea surface temperatures associated with the oceanic front, 2) the Andes and Antarctica, which can modify the large-scale flow within which these cyclones form, 3) the sea-ice boundary, which allows the cold Antarctic air to become very unstable when exposed to the sensible and latent heat fluxes over the open ocean, and 4) internal dynamic instabilities associated with the two branches of the westerlies.

In early September 1987, one such storm developed over the South Pacific Ocean, deepening rapidly as it approached the periphery of Antarctica. One indication of the intensity of this storm was the strong upward transport of low ozone air to the tropopause on the eastern side of the trough, which produced a very pronounced ozone minimum ("minihole") over the Palmer Peninsula (Orlanski et al. 1989; McKenna et al. 1989). The purpose of this paper is to investigate the contributions to cyclone development in the South Pacific through numerical simulations of this explosive cyclone. In the following section, a synoptic description of the storm using the European Centre for Medium Range Weather Forecasts (ECMWF) analysis is given. In section 3, a numerical simulation of the storm is presented and verified against the analysis. Using the simulation, trajectory diagnostics are computed to describe the structure and evolution of the storm. In section 4, the relative importance of topography and surface forcing in the development of the cyclone is investigated through a series of sensitivity experiments. A summary of the results is presented in section 5.

2. Data

a. Synoptic description

The storm that is the subject of this investigation occurred over the South Pacific west of the Palmer Peninsula on the periphery of the Antarctic plateau on

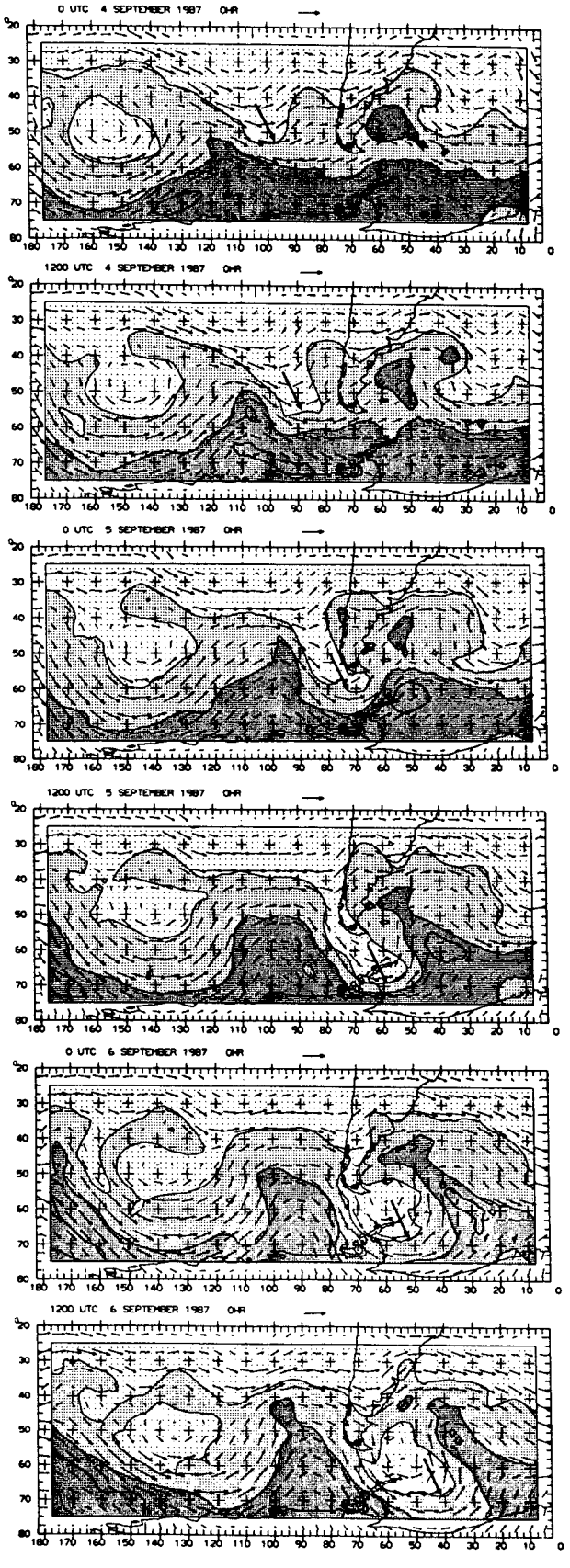

4–6 September 1987. The following description of the storm is based on the 7-level ECMWF 2.5° by 2.5° global analysis. For convenience, we will confine our descriptions of events to the region from 118° to 31°W and from 30.5° to 80°S, which corresponds to the domain of the limited-area model simulation to be described later. The time period analyzed in this paper is from 1200 UTC 4 to 1200 UTC 6 September 1987, the period of explosive development and maturation of the storm. Analysis of the earlier development and its relationship to the planetary flow will be published elsewhere.

Inspection of the potential vorticity (PV) field during this period will help to clarify the origin and evolution of the cyclone wave. Figure 2 shows the distribution of potential vorticity,

$$\mathrm{PV} = -g\left(\frac{\partial p}{\partial \theta}\right)^{-1}(\zeta + f),$$

and the velocity vectors on the 320 K isentropic surface at 12-h intervals from 0000 UTC 4 to 1200 UTC 6 September. The domain has been centered approximately on the area of most rapid evolution of the wave for that period. Three bands of PV have been shaded in order to highlight the subtropical and high-latitude PV. The western high at 150°W (with low magnitude, negative PV) is readily identifiable, but equally important is the large intrusion of low-magnitude PV from the subtropics to the sub-Antarctic region near 90°W at 1200 UTC 4 September. This subtropical potential vorticity was advected poleward ahead of an eastward moving high-latitude wave and its associated subpolar potential vorticity minimum. The low PV values from the subtropics became trapped in the anticyclonic circulation of the ridge downstream from the high-latitude wave. The initial state, characterized by a rather zonal field with mainly meridional gradients of PV, becomes progressively more contorted, with large PV anomalies intruding from the subtropics and subpolar regions.

The vertically averaged 30-day mean wind for September 1987, again using the ECMWF analyses, is shown in Fig. 3a. The subtropical jet (STJ) originates over the central Indian Ocean (75°E) and reaches maximum intensity over the South Pacific Ocean (160°W). Near South America, the axis of the jet begins to spiral in toward the pole, producing a dual jet structure, which extends from the Indian Ocean to South America. A cross section of the zonally averaged potential temperature and zonal wind for the sector between 118°W and 74°W is shown in Fig. 3b for 1200

FIG. 2. Ertel potential vorticity and wind vectors on the 320 K isentropic surface at 12-h intervals, from 0000 UTC 4 September to 1200 UTC 6 September. Dark, medium, and light shading correspond to regions of less than -4×10^{-6}, -4 to -2×10^{-6}, and greater than -2×10^{-6} m^2 K s^{-1} kg^{-1}, respectively. Arrow at top of panels indicates wind speed of 10 m s^{-1}.

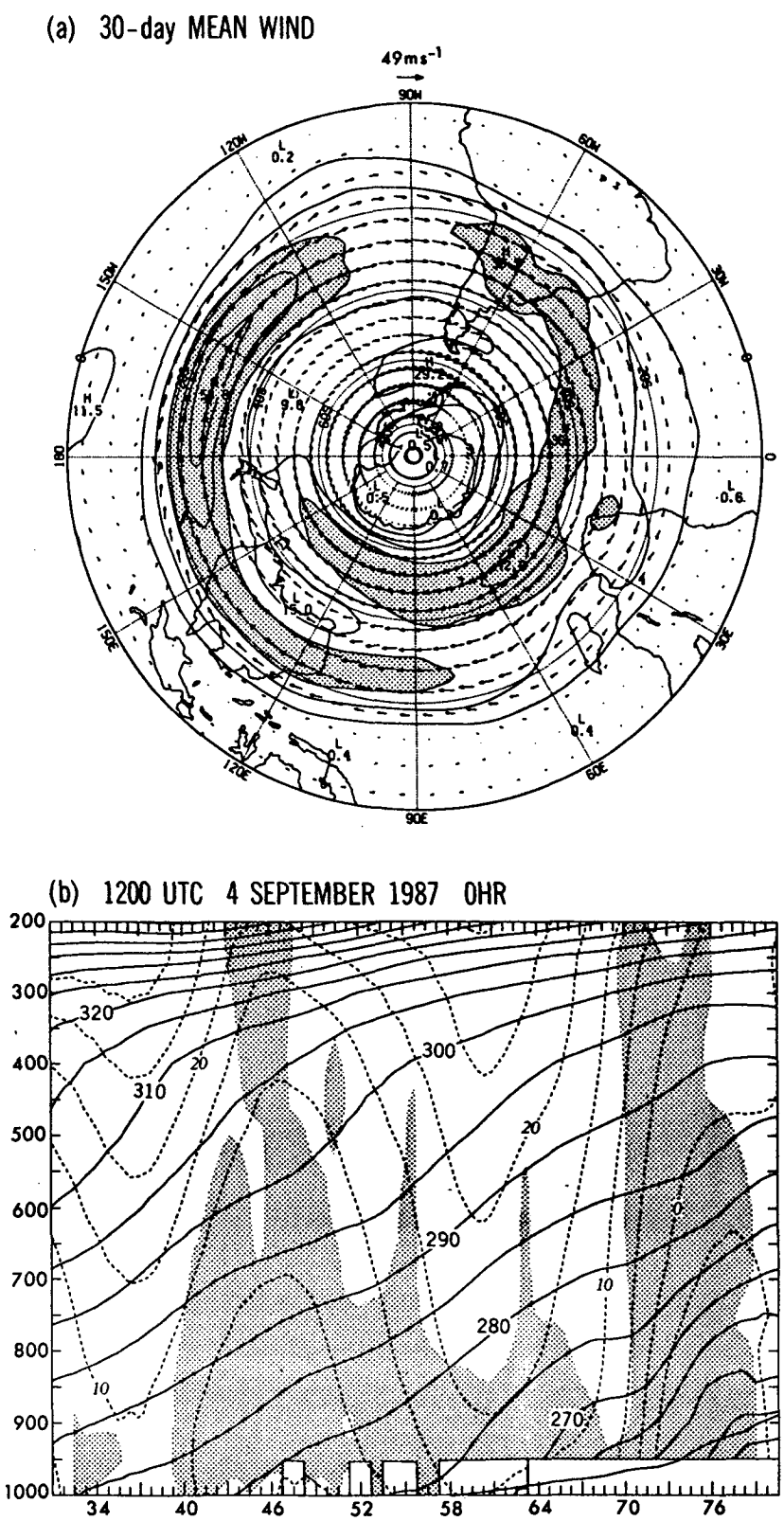

FIG. 3. (a) Vertically averaged September 1987 30-day mean wind. Wind speed interval is 10 m s^{-1}, greater than 30 m s^{-1} shaded. (b) Sector average (118° to 31°W) of potential temperature (solid, every 5 K) and zonal wind (dashed, every 5 m s^{-1}) for 1200 UTC 4 September. Regions with negative meridional gradient (on isentropic surfaces) of PV are shaded. Abscissa is degrees south latitude.

UTC 4. The dual jet structure is evident in the cross section, with the STJ located near 40°S and the polar jet (PJ) located near 60°S. One characteristic frequently used to detect potential barotropic or baroclinic instabilities in zonal flows is a change in the sign of the meridional gradient of the potential vorticity (Charney and Stern 1962). Regions with negative meridional gradient of PV on isentropic surfaces are shaded in Fig. 3b, indicating that there was indeed a large vertical zone of negative meridional gradients of potential vorticity and associated sign reversals.

The flow aloft (not shown) prior to 1200 UTC 4 had been primarily zonal over the South Pacific, with separate wind maxima associated with the PJ and the STJ. By 1200 UTC 4, significant meridional flow was developing as the flow became distorted, with the STJ migrating poleward and merging with the PJ. Significant baroclinicity was evident at the base of the trough. As suggested by the evolution of PV on the isentropic surfaces (Fig. 2), the PJ was entering the western side of the trough (130°W) poleward of 50°S with southwesterly winds, while the STJ was located equatorward of 45°S with northwesterly winds. This merger was followed by the development of the strong ridge east of the trough by 1200 UTC 5 (see arrow, Fig. 2).

Figure 4 shows the ECMWF analyses of mean sea level pressure, along with the vertical component of the surface relative vorticity for the period between 1200 UTC 4 and 0000 UTC 6 September 1987. Four main cyclonic systems were evident at the surface at 1200 UTC 4. The first system was located just off the Antarctic continent near 100°W (system A). This was a deep cyclonic wave with very little vertical tilt (i.e., equivalent barotropic) propagating within the polar branch of the westerlies (the PJ). A smaller-scale cyclonic disturbance (system B) was located at 53°S, 100°W on the northern edge of the cyclone wave. This disturbance was previously a shallow system moving eastward within the subtropical branch of the westerlies. Strong poleward flow is evident at low levels east of systems A and B. Two more cyclonic disturbances were located over the South Atlantic east of South America (system C) and just off Antarctica (system D).

During the early stage of development, the polar wave (system A) intensified and merged with the disturbance within the STJ (system B). The merger of these two systems allowed warm, moist subtropical air to move poleward, creating strong baroclinicity. After 1200 UTC 4, the two systems developed jointly in a manner similar to Pettersen and Smebye (1971) type B cyclogenesis and, as described by Hoskins et al. (1985), with the upper wave from the polar westerlies interacting with a lower-level baroclinic zone produced by the confluence of polar and subtropical air masses.

The sea level pressure minima for systems A and B are plotted in Fig. 5, together with the maximum of the vertically averaged kinetic energy (in the neighborhood of the two centers). The central pressure of system B (taken at the point of maximum surface vorticity) was initially 984 mb, but dropped dramatically as the system moved southeastward and intensified during the ensuing 24 h, reaching 952 mb after merging with system A by 1200 UTC 5. This rapid development is similar to that exhibited by explosive cyclones over the eastern North Pacific (for example, see Reed 1979; Reed and Albright 1986, hereafter referred to as RA-86). Strong poleward flow throughout the troposphere east of this system contributed to a significant increase in the height of the ridge located downstream of the trough. The storm was accompanied by strong surface winds (greater than 30 m s^{-1}) and deep convection along the frontal zone. The intensification is also evident in the kinetic energy, which increased from 600 m^2 s^{-2} at 1200 UTC 4 to 950 m^2 s^{-2} over a 24-h period. Satellite imagery of this region taken at 0143 UTC 6 (not shown here) showed a cloud signature that was characteristic of an intense extratropical cyclone, with warm, moist, cloud-laden air spiraling into the center of the cyclone from ahead of the storm and colder, drier air being drawn into the storm from the rear—a circulation similar to that exhibited by North Pacific storms (RA-86).

b. *Numerical model*

The foregoing qualitative description was based on 12-h ECMWF analyses. However, the higher spatial and temporal resolution and more dynamically consistent fields available from an accurate model simulation will make possible a more detailed and quantitative investigation of the storm's structure, particularly over the data-sparse ocean.

The numerical model used in this study is the GFDL version of the Limited Area HIBU[1] Model with the GFDL physics package [LAHM–GFDL, see Orlanski and Katzfey (1987) for a more complete description of the model]. The LAHM model is a primitive equation sigma coordinate model with either 9 or 18 vertical levels, employing a latitude–longitude E grid with a grid spacing (in this case) of 0.75° latitude and 1.5° longitude, which preserves similar spatial separation at high latitudes. The model physics is similar to the E2 physics package of GFDL (Miyakoda and Sirutis 1977) and includes radiation, Arakawa and Schubert convective parameterization, and soil and sea-ice surface parameterizations. The lateral boundary conditions utilize time tendencies of the dependent variables interpolated in time and space from the 2.5° by 2.5° ECMWF analysis. The model was initialized at 1200 UTC 4 September by interpolation from the ECMWF analysis, with hydrostatic adjustment of the temperature field. Sea surface temperatures are derived from the September monthly mean climatological values.

[1] Federal Hydometeorological Institute and Belgrade University.

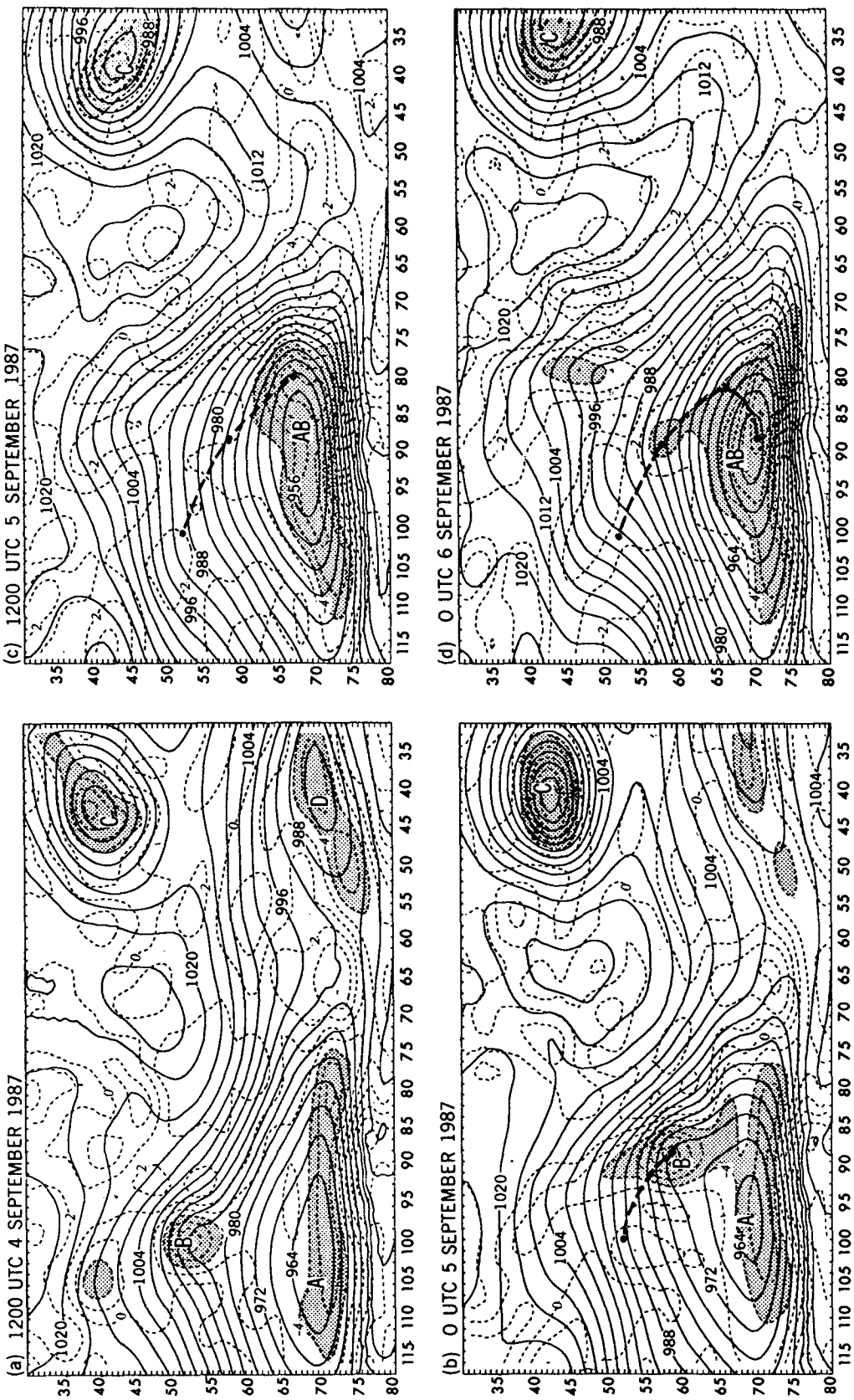

FIG. 4. Analysis, from ECMWF data, of sea level pressure (solid lines, every 4 mb) and lowest model sigma layer (i.e., lowest 80 m) relative vorticity (dashed lines, interval: 2×10^{-5} s^{-1}, values in excess of -4×10^{-5} s^{-1} shaded). Letters indicate primary cyclonic disturbances, and the path of system B is indicated by heavy dashed line.

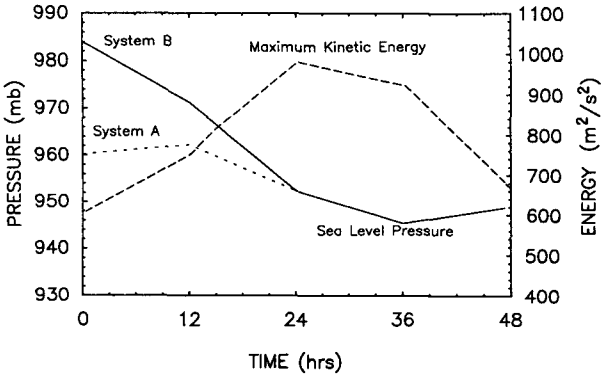

FIG. 5. Time evolution of analyzed sea level pressure (solid line is system B, short dashed line is system A) and maximum kinetic energy (long dashed line) based on ECMWF data. Horizontal axis is time, in hours, after 1200 UTC 4 September.

Comparison with September 1987 values showed no significant differences from climatology in either the sea surface temperatures or the sea-ice boundary.

3. Model diagnostics

In this section, the model simulation of the 4–5 September storm (system AB) is verified against the ECMWF analysis. Cross sections are used to show the vertical structure of the storm, and trajectory analyses illustrate the displacement of air parcels.

a. The simulation

The 48-h, 9-level model simulation, initialized at 1200 UTC 4 September, successfully captured the salient features of the storm development. Figure 6 shows the mean sea level pressure, the temperature, and winds in the lowest sigma level of the model, as well as the heights, temperatures, and winds at 500 mb for 24 and 48 h into the simulation. In general, the location of the various features in the simulation compare favorably with the analysis. The development of the small wave in the initial analysis (system B in Fig. 4) into a large system, as it merged with system A, was reasonably well simulated, considering the coarseness of the analysis and the sparseness of data over oceanic regions and Antarctica. The intensification of the ridge over Drake Passage was also captured. System AB was slightly northeast of the analysis in the simulation and not as deep. However, the low-level winds were fairly well simulated. This was also true at 48 h, although system AB was weaker and farther east than observed at all levels. The secondary system near 50°S, 90°W was also evident in the simulation. The depth of the wave at 500 mb in the west was slightly underestimated and east of the analysis.

Over the ocean, the air temperature near the surface was strongly controlled by the sea surface temperature and did not reflect the frontal occlusion that developed after 24 h. However, the 850-mb temperature (see Fig. 7a) is less affected by surface conditions and clearly shows the beginning of the occlusion stage at 24 h, with the warm air becoming wrapped around the low. The vertical component of relative vorticity (Fig. 7b) and the vertical vorticity, ω, (Fig. 7c) at 850 mb portray the primary front as a region of strong negative vorticity (analogous to positive vorticity in the Northern Hemisphere) and ascent. System C (over the Atlantic) is evident in the vorticity pattern, but lacks significant vertical motions at this time. Note also a hint of the vertical circulation associated with the secondary system near 50°S, 100°W.

b. Cross sections

Figure 8 shows vertical cross sections of wind and potential temperature at 0, 12, and 24 h into the simulation along line AA′ shown in Fig. 7b. The vertical structure across the front is evident in the contours of potential temperature and the perpendicular wind component, and also in the vectors indicating the cross-stream circulation.

The cross section at 12 h (Fig. 8b) displays the best example of a typical frontal circulation, possibly because the cross section was more perpendicular to the front at this time compared to the other times. One can see the basic frontal characteristics, such as the upper-level jet near 300 mb, the equatorward surface winds in the cold air south of the front, and a poleward low-level jet on the warm side of the front, similar to that found in Orlanski et al. (1985). Two main features stand out in association with this front. First, the front does not tilt with height, with the upper-level jet located almost directly above the surface front. Second, weak static stability exists ahead of the front between 500 mb and 300 mb. A lack of frontal tilt was also noted by RA-86 in a case of an explosive storm that developed in the North Pacific. It is possible that intense frontal development over the oceans may have a larger barotropic component than that over land due to lower surface friction. Many of the characteristics of this cyclone are similar to those reported by RA-86. In the North Pacific case, development took place within a strong baroclinic zone, as a shallow frontal wave traveled from the relatively stable environment of a long-wave ridge to the unstable environment of a long-wave trough. In this case, a shallow disturbance in the subtropics migrated poleward to the eastward side of a polar wave.

The pronounced weak static stability of the upper-tropospheric air on the anticyclonic side of the jet is also a notable feature associated with this front. Inspection of the 500-mb geopotential heights, temperature, and winds at 24 h (Fig. 6) shows that this upper-tropospheric pocket of low static stability was caused by strong warm air advection associated with the poleward migration of the STJ. Low static stability in the

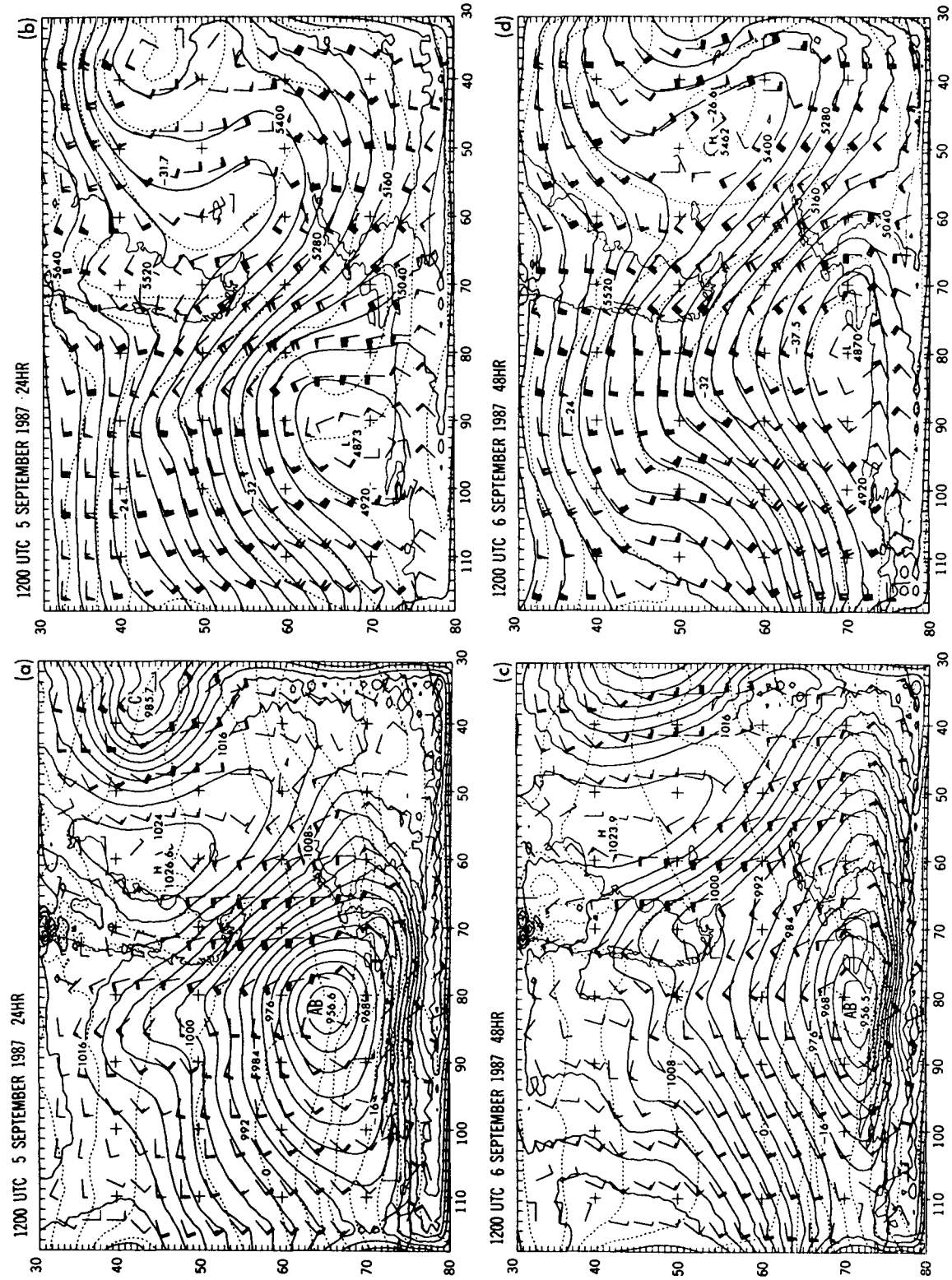

FIG. 6. Model simulation. Left panels: sea level pressure (solid, every 4 mb), temperature (dashed, every 4°C) and winds in lowest sigma level (0.99555); right panels: geopotential heights (solid, every 60 m), temperature (dashed, every 4°C) and winds at 500 mb. Times are 1200 UTC 5 September (24 h, top) and 1200 UTC 6 September (48 h, bottom). Winds plotted with half barb = 2.5 m s^{-1}, full barb = 5 m s^{-1}, flag = 25 m s^{-1}.

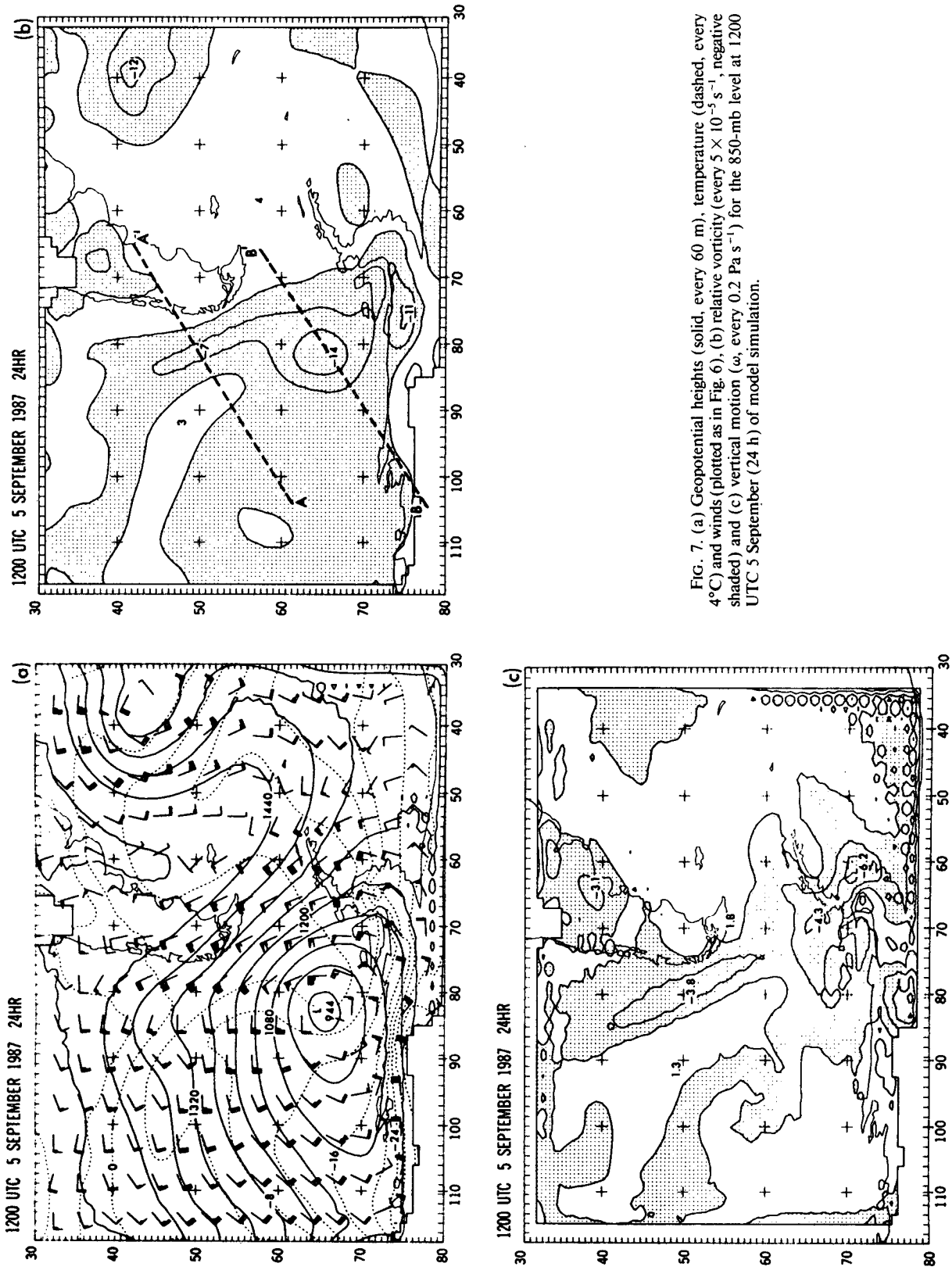

FIG. 7. (a) Geopotential heights (solid, every 60 m), temperature (dashed, every 4°C) and winds (plotted as in Fig. 6), (b) relative vorticity (every 5×10^{-5} s^{-1}, negative shaded) and (c) vertical motion (ω, every 0.2 Pa s^{-1}) for the 850-mb level at 1200 UTC 5 September (24 h) of model simulation.

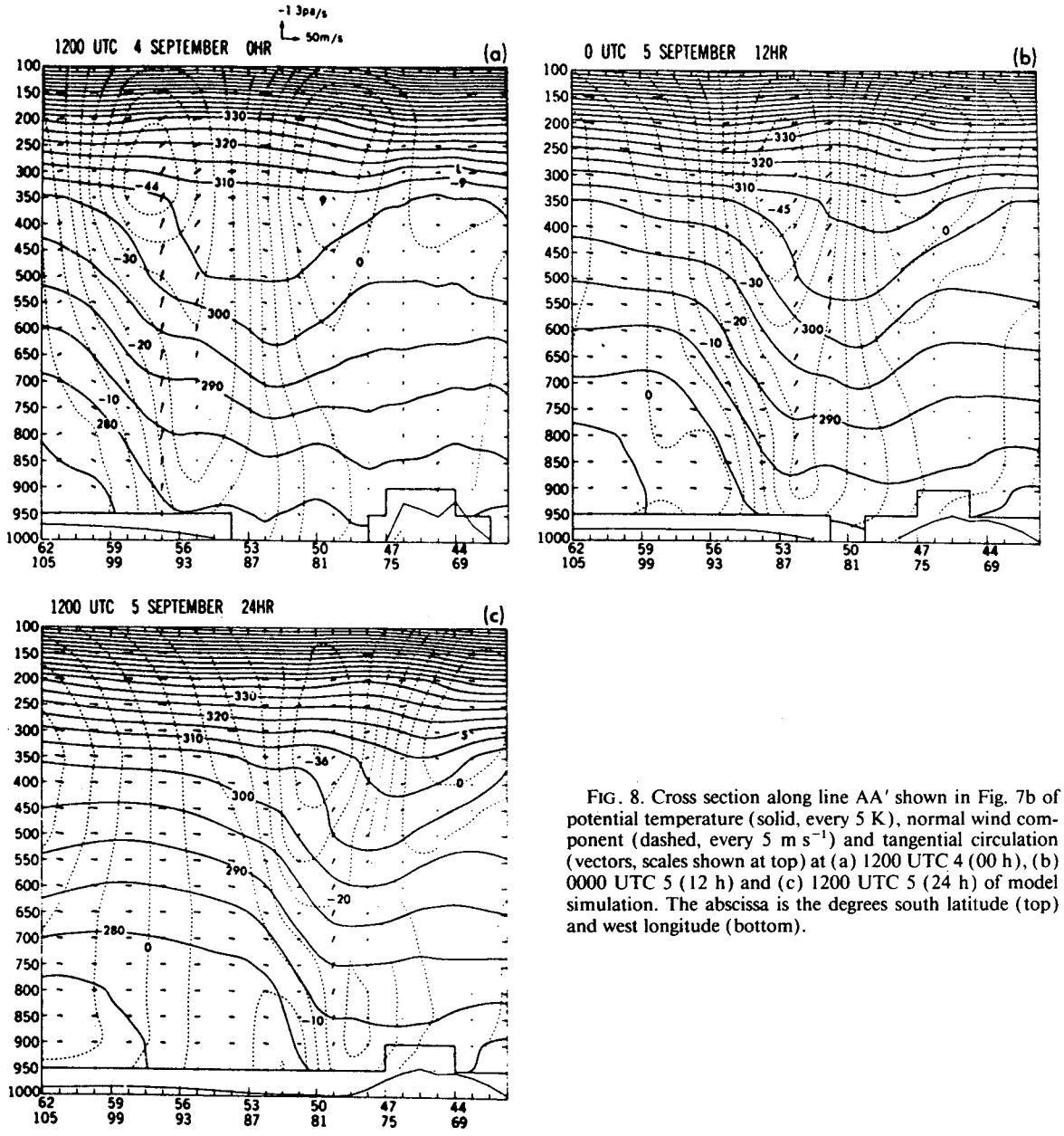

FIG. 8. Cross section along line AA′ shown in Fig. 7b of potential temperature (solid, every 5 K), normal wind component (dashed, every 5 m s^{-1}) and tangential circulation (vectors, scales shown at top) at (a) 1200 UTC 4 (00 h), (b) 0000 UTC 5 (12 h) and (c) 1200 UTC 5 (24 h) of model simulation. The abscissa is the degrees south latitude (top) and west longitude (bottom).

upper troposphere is also occasionally observed for storms that develop in the North Atlantic (Hoskins and Berrisford 1988).

c. *Lagrangian trajectories*

To provide additional insight into the development of the storm, trajectories were calculated using the horizontal winds and vertical motion fields from the simulation. Each parcel was initialized with the simulation horizontal wind and vertical motion. The position of the parcel was then integrated forward in time iteratively using the average of the initial parcel velocities and the parcel velocities interpolated from the model fields at the end of the 9-minute time step. The iteration was repeated until the position of the parcel at the end did not change. The integration is then continued using the new parcel position and velocities as starting values for the next time step.

A very large number of parcels should be tested in order to give a comprehensive, coherent picture of the time evolution of a storm system such as this one. Over 100 parcel trajectories were computed, and the trajectories of the seven parcels that most clearly capture the

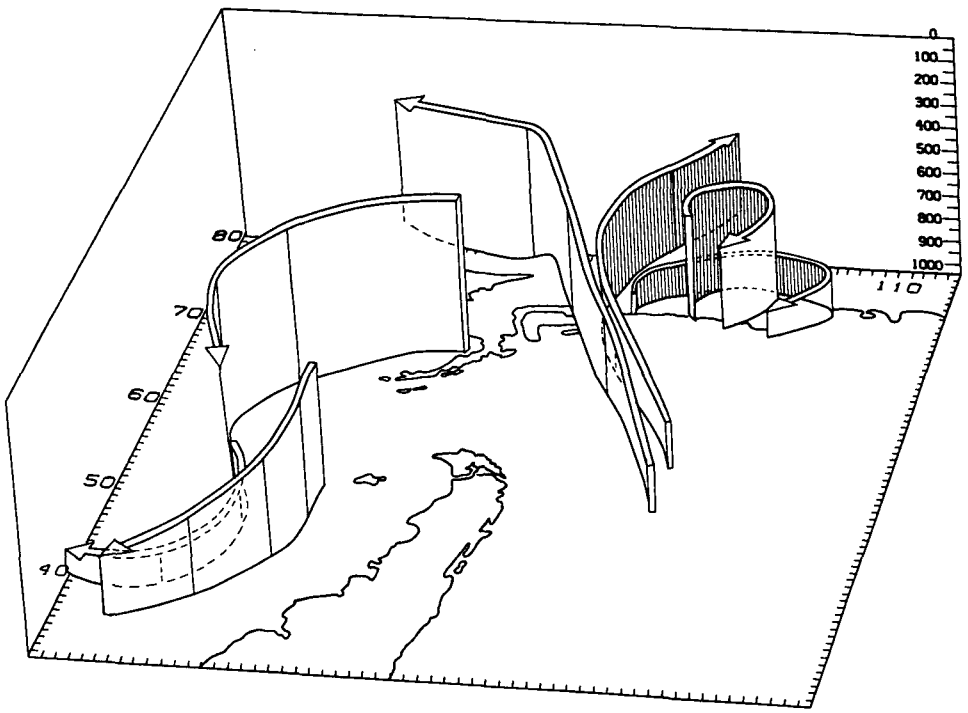

FIG. 9. Lagrangian trajectories, computed using model-simulated winds, for a 24-h period starting at 1200 UTC 4 September for parcels originating at 950 mb, 850 mb, and 500 mb.

structure of the storm are shown in Fig. 9, originating at 850 mb, 700 mb, or 500 mb for different geographic locations and integrated from 00 to 24 h. The view in this (3D) figure is toward the Antarctic continent. The two parcels starting over the Pacific Ocean west of the Drake Passage (about 55°S, 850 mb) were caught up in the strong flow of rising air along the frontal zone. However, the parcel initialized nearer the pole curved cyclonically around the cyclone while the other parcel curved anticyclonically in the downstream ridge, illustrating the bifurcation of the ascending flow as it reached the Antarctic continent, as noted in the 500-mb maps (Fig. 6b,d).

The strength of the vertical advection in the frontal region is evidenced by a strong minimum in the total (column-integrated) ozone content measured by the Total Ozone Mapping Spectrometer (TOMS). The TOMS measurements are markedly different from ozone measurements made in frontal regions in the Northern Hemisphere (Shapiro 1980; Uccellini et al. 1985), where a *maximum* of total ozone content was found within the frontal zone. In fact, it has been observed that the Antarctic ozone hole is constantly punctuated by miniholes produced on the periphery of the Antarctic continent by storms such as this one (Orlanski et al. 1989; McKenna et al. 1989), with low ozone air from the lower troposphere being transported up to the tropopause level. A more complete discussion of the effects of sub-Antarctic cyclones in the daily variability of the ozone content in the region will be published elsewhere.

The trajectories of two parcels initialized at 850 mb and 500 mb over the coast of Antarctica (see Fig. 9) illustrate the cyclonic circulation of system A. The parcel that started at 500 mb over the Palmer Peninsula moved northeastward, gliding down the eastern side of the ridge toward system C. The circulation around system C and the descent west and equatorward of the system can be seen in the trajectories of the two parcels originating over the Atlantic.

4. Orographic and surface forcing

Several hypotheses have been put forward suggesting the importance of surface processes in the development of cyclones in this region. Given that this storm formed over the open ocean, it is reasonable to suspect that surface heat fluxes may have been important. In addition, the development of strong poleward flow just upstream of the Andes suggests a possible topographic influence. Having established that the model is capable of reproducing the essential features of this storm, we may, with some confidence, test some of these hypotheses through a series of sensitivity experiments. A summary of the experiments to be discussed in this section is shown in Table 1.

TABLE 1. Summary of sensitivity experiment parameters.

	Case designation					
	z_0 Land (cm)	Ocean "α" $z_0 = \alpha^* V^2/g$	Heat fluxes (on/off)	Momentum fluxes (on/off)	Earth surface	South American topography (yes/no)
Control	16.82	0.032	On	On	Land/ocean	Yes
No-Andes						No
No heat fluxes			Off			
No momentum fluxes				Off		
All land					Land only	
All land, $0.01^* z_0$	0.1682				Land only	
$0.01^* z_{0,\ \text{land and ocean}}$	0.1682	0.00032				

a. *Orographic effects*

The weather of the eastern South Pacific region can be strongly affected by the Andes. Figure 10 shows the "effective cross section" of the Andes, defined as the maximum topography for each latitude belt between 90° and 50°W. Three resolutions were chosen to illustrate the effective cross section of the mountain barrier for a typical global model resolution (3°), typical mesoscale model resolution (1°), and the resolution of the Navy topography data used (1/6°). It is apparent that while the low tropospheric flow can be significantly influenced by the mountain barrier, a lower-resolution global model, by seeing a less effective barrier, probably will not be influenced as much by the South American continent, thereby inaccurately forecasting the weather in this region.

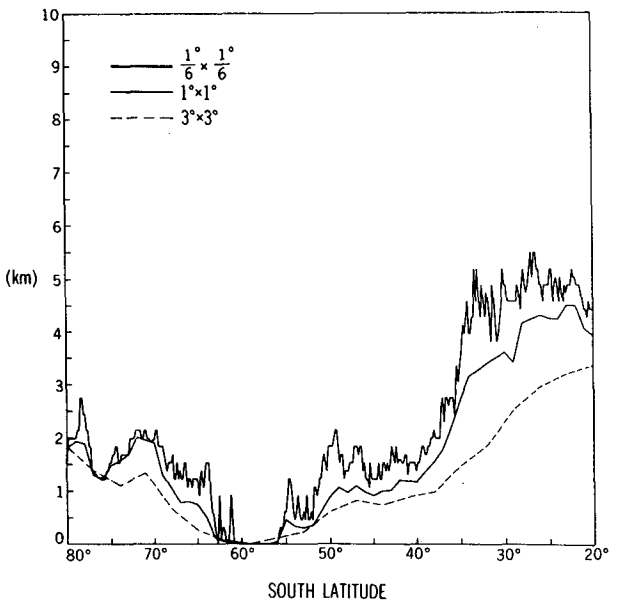

FIG. 10. Silhouette orography between 90° and 50° for three grid spacings.

A simulation was performed without orography north of 70°S using the 18-level version of the LAHM initialized with the ECMWF analysis at 1200 UTC 4 September in order to test the impact of the flow over and around the Andes Mountains. This "No-Andes" solution is compared to an 18-level "Control" model run with topography. (The results of the Control run were similar to the 9-level model results discussed so far, and are not shown.) The land points in the no-Andes run were not changed to sea points when the orography was removed, so the surface temperatures predicted over the South American continent were similar to the control run. As in the Control, land temperatures were cooler than the surrounding oceans, since this is a Southern Hemisphere winter case.

In general, the No-Andes simulation showed few differences from the Control. Throughout the simulation there was less than 1 mb difference in the minimum mean sea level pressure between the simulations. However, slight differences in the development of the storm are evident in Fig. 11, which shows the time

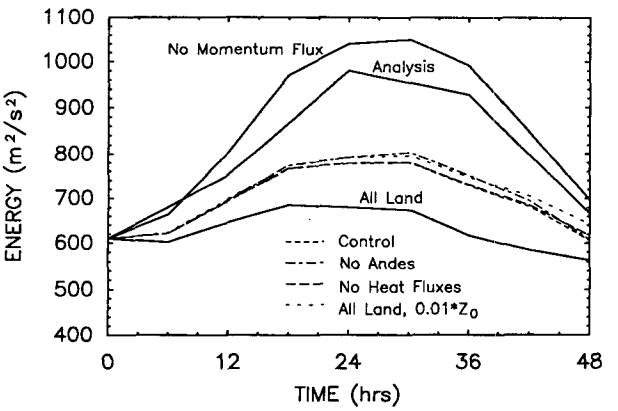

FIG. 11. Temporal evolution of maximum vertically averaged kinetic energy from ECMWF data (Analysis), No Momentum Flux simulation, All-Land simulation (solid), plus four additional simulations: Control (medium dash), No-Andes (dash-dot), No Heat Fluxes (long-dash) and All-Land, $0.01^* z_0$ (short dash).

evolution of the maximum vertically averaged kinetic energy. In general, the kinetic energy for both cases grew until 30 h and decreased thereafter. Of the two cases, the control simulation had a slightly larger deficit of kinetic energy compared to the analysis, with the maximum difference corresponding to about a 3.5 m s^{-1} weaker vertically averaged wind. The kinetic energy for the No-Andes case became slightly larger than the Control after 6 h, long before the cyclone itself neared the Andes, and this difference increased until 30 to 36 h. After 36 h, the kinetic energy of the No-Andes case decreased somewhat faster than the Control so that by 48 h the energies were once again similar. These results indicate that although the presence of the Andes did not have any major impact on the development of the storm, they did have a minor effect on the generation of kinetic energy even when the storm was well upstream of the mountain range.

b. *Surface forcing*

The precise role of surface heat fluxes on cyclogenesis has been a subject of debate for quite some time. Recently, Kuo and Low-Nam (1990) reviewed and discussed in some detail the impact of surface energy fluxes. Many studies indicated that surface heat fluxes in the cold air behind the cold front will tend to destroy the temperature contrast and therefore represent a negative influence on cyclone development. Other studies have pointed out the importance of the surface fluxes of heat and moisture in preconditioning the lower troposphere, making it less stable and more conducive to eventual development, as in cases of coastal cyclogenesis (e.g., Bosart and Lin 1984; Orlanski and Katzfey 1987; and others).

The surface fluxes of heat and moisture in the Control simulation are shown in Fig. 12 for 6 and 48 h. The largest latent heat fluxes are found over the South Atlantic Ocean in association with system C. The fluxes associated with storm AB initially tend to be very weakly positive in the cold air behind the cold front, but become markedly larger as the storm intensifies and draws cold air off the Antarctic continent and out over the relatively warm ocean. Small negative sensible heat fluxes occur in the region of warm advection ahead of the cyclone. The resulting decreased temperature contrast will tend to *hinder* further development for storm AB. On the other hand, inspection of the trajectories shown in Fig. 9 suggests that some parcels near the low center recirculate, moving equatorward and sinking west of the low. In doing so, they pick up heat and moisture from the surface in the regions of larger fluxes and then move poleward and rise, releasing their energy through condensation. This process could constitute a positive feedback mechanism by which the surface fluxes behind the low might aid storm development. At the very least, the surface fluxes will mitigate the negative influence of cold air entrainment into the cyclone.

In an effort to determine whether either of these effects (negative or positive) dominate, a simulation was run in which the surface heat fluxes were turned off (NHF, No Heat Fluxes). The resulting time evolution of the maximum vertically averaged kinetic energy, shown in Fig. 11, indicates that surface heat fluxes had virtually no net impact on the overall kinetic energy of the storm.

To evaluate the possible differences in the effects of heat fluxes over the ocean (where surface temperature is held fixed) and fluxes over land (where heat balance requirements determine surface temperature), two simulations were run in which the ocean surface was replaced with land surface (All-Land). In the first case, the roughness height, z_0, was set to a characteristic land value of 16.82 cm, the default value used for land surface in the model. Surface temperatures were initialized to sea surface values, and soil moisture was initialized to zero. The resulting kinetic energy of the storm was reduced markedly from the Control, as shown in Fig. 11. In the second All-Land case, z_0 was reduced by a factor of 100, thereby lowering it to a value typical of a moderately rough sea (ocean z_0 is a function of wind speed in the model), and the kinetic energy levels rose to values similar to the Control. Evidently, surface friction has more profound effects on the intensity of this storm than do surface heat fluxes.

Because surface friction appeared to have such a large impact on the storm's kinetic energy, another simulation was run in which momentum fluxes from the surface (i.e., drag) were turned off (NMF, No Momentum Fluxes). The result was a striking increase in the kinetic energy levels (see Fig. 11), surpassing that of the analysis. Cross sections through the frontal region (A-A′ in Fig. 7b) are somewhat more revealing with respect to the effects of the various types of surface forcing. Figure 13a shows the potential temperature and vertical velocity, ω, for the Control at 30 h. Figures 13b, 13c, and 13d show the potential temperature and the difference of ω with the Control for the All-Land, NMF, and NHF simulations, respectively. The Control solution is typical of cold fronts, as discussed in section 3b. Strong upward motion (negative ω) is found ahead of the strongest horizontal potential temperature gradients, and descending motion is found on the cold side of the front. Note that the temperature gradients on the cold side of the front are rather weak, due primarily to sensible heating by the ocean surface. In contrast, the All-Land and NHF cases exhibit considerably larger temperature gradients on the cold side of the front. In the NHF case, this stronger gradient is obviously due to the lack of surface-layer modification of the cold air by heat fluxes, and the surface-layer baroclinicity is maintained. In the All-Land case, rapid cooling of the ground surface greatly reduces surface

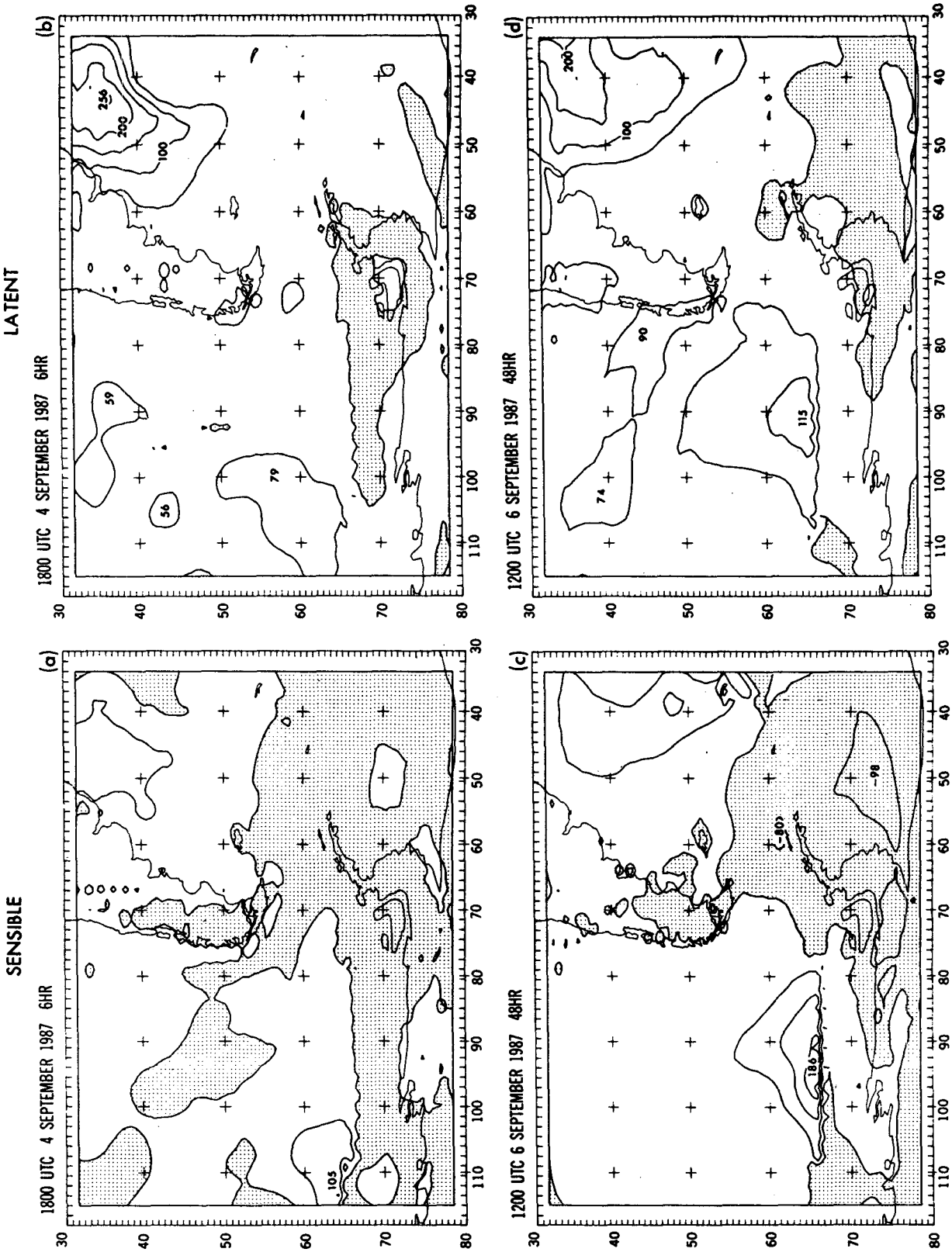

FIG. 12. Surface heat fluxes: sensible [(a) and (c)] and latent [(b) and (d)] at 6 h, 1800 UTC 4 September [(a) and (b)] and 48 h, 1200 UTC 6 [(c) and (d)] (every 50 W m^{-2}, negative values shaded).

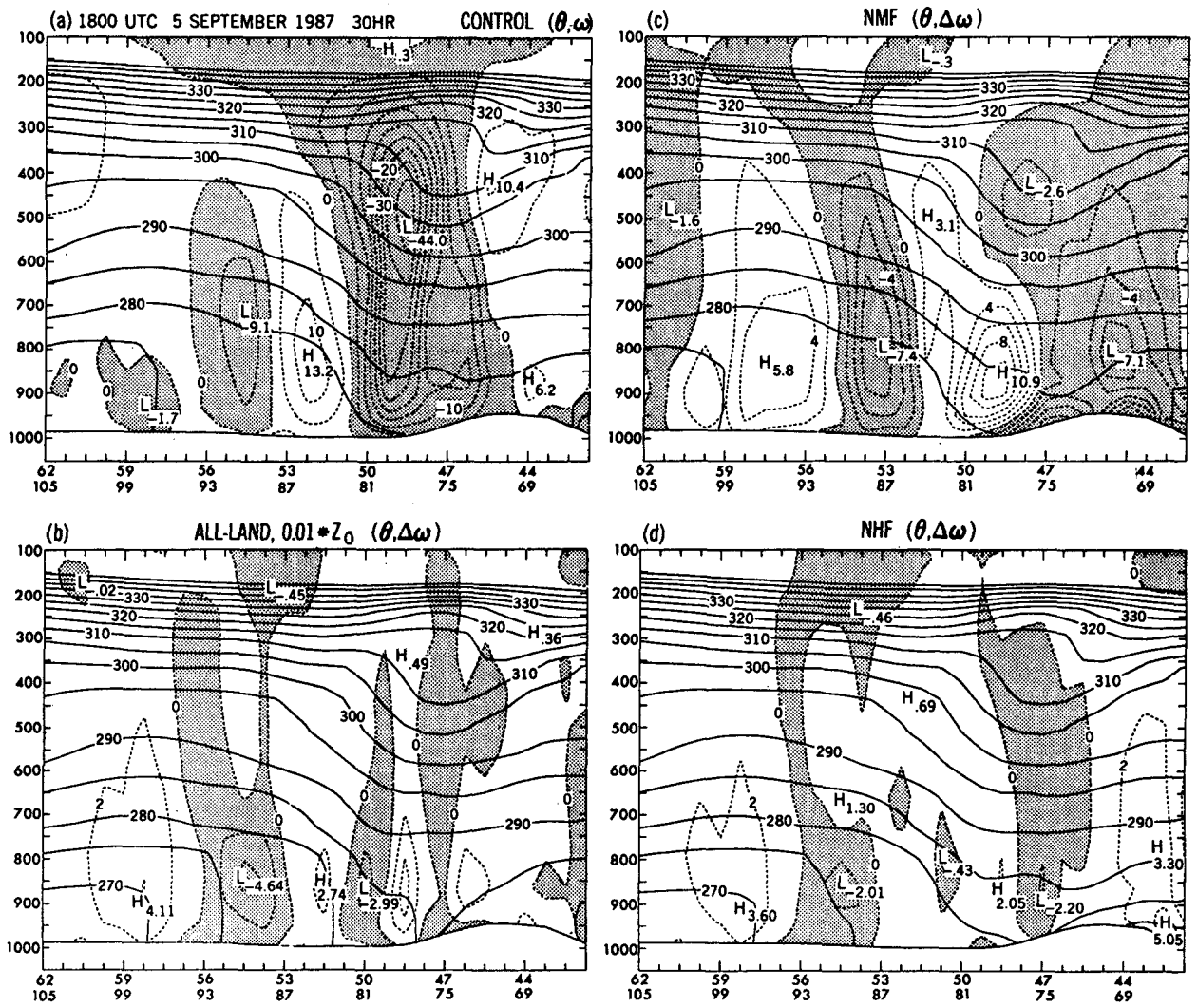

FIG. 13. Cross sections at AA′ (see Fig. 7b) of potential temperature and vertical velocity, ω, at 1800 UTC 5 September (30 h into simulation). Solid lines are potential temperature (every 5 K). Dashed lines in (a) are Control ω (every 0.05 Pa s^{-1}, negative values are shaded indicating upward motion). Dashed lines in (b), (c), and (d) are ω difference (every 0.02 Pa s^{-1}) from Control for the All-Land; 0.01*z_0, NMF, and NHF cases, respectively. Abscissa as in Fig. 8.

heat fluxes, yielding the same qualitative result. What is more important in these two cases is that their differences from the control are limited almost entirely to the temperature field in a shallow boundary layer, while the kinetic energy, vertical motions, and other dynamics are virtually unchanged. It would therefore appear that the common belief that oceanic fronts will be less intense than those over land in winter may need to be reexamined. Even in this case, which includes strong modification of frigid Antarctic air over the South Pacific, the effects are limited to the temperature field in the boundary layer.

In contrast, the NMF case exhibits considerable differences in the dynamics of the storm, but rather small changes in the temperature field (Fig. 13c). The absence of momentum fluxes at the surface produces direct changes not only in the boundary layer but also throughout the troposphere. The magnitude of the boundary-layer vertical velocities have been reduced in both ascending and descending branches of the frontal circulation, probably due to the absence of Ekman pumping in the NMF case. In the middle to upper troposphere, the vertical velocities have increased, consistent with the overall increased intensity of the storm and similar to the results for a baroclinic system without surface drag, as found by Valdes and Hoskins (1988).

Overall, this storm displayed much greater sensitivity to surface friction effects than to surface heating effects, as reflected in the fact that the All-Land, high z_0 simulation produced a much larger response than either using an ocean surface or shutting off the heat fluxes

entirely. In particular, the dramatic increase in kinetic energy resulting from the removal of surface drag is especially interesting given that this storm evolved almost entirely over open water. Since the default values of z_0 for the ocean and land parameterizations used here are typical of most numerical models, even those used operationally by ECMWF and NMC, this issue deserves somewhat closer examination with respect to its impact on the simulations.

c. *Roughness height*

The importance of surface friction for this case was evaluated further by performing two additional experiments in which the surface roughness values for land, $z_{0,\text{land}}$, and ocean, $z_{0,\text{ocean}}$, were reduced (see Table 1). Although the track of the storm in both cases was similar to the control, use of a lower z_0 over the ocean produced minimum sea level pressures that were much more in line with the analyses. Figure 14 shows the minimum sea level pressure every 3 h for the control, as well as the NMF case and cases with $0.01*z_{0,\text{land}}$ and $0.01*z_{0,\text{land and ocean}}$. The minimum sea level pressure for the analysis is plotted at 12-h intervals. As expected, the NMF case shows the largest deviation from the control, reaching a minimum sea level pressure 20 mb deeper than the control and 10 mb deeper than the analysis. The case with $0.01*z_{0,\text{land}}$ shows little difference from the Control for the first 30 h, then deepens by an additional 5 mb when the storm is near the Antarctic ice sheet. The case with $0.01*z_{0,\text{land and sea}}$, however, develops lower pressure throughout the entire period, deepening by an additional 5 mb over the first 30 h and another 5 mb during the next 6–9 h, similar to the case with $0.01*z_{0,\text{land}}$.

The maximum vertically averaged kinetic energy for each of these cases is plotted in Fig. 15, and shows, not surprisingly, that the decrease in surface friction associated with the decrease in z_0 produced higher wind speeds and kinetic energies, at least on a vertically averaged basis. Insight into the vertical distribution of the kinetic energy deficiencies of the simulations is provided by Fig. 16, which shows a cross section (B-B′ in Fig. 7b) of the difference in kinetic energy between the ECMWF analysis and the Control case. From this it is seen that the kinetic energy deficit is not limited to the surface layers where friction would have the most direct impact, but extends throughout the depth of the troposphere. (There is a slight phase difference between the two fields, but on balance, there is a net deficit in the Control.) Figure 17 shows the vertical distribution of the change in kinetic energy from the Control

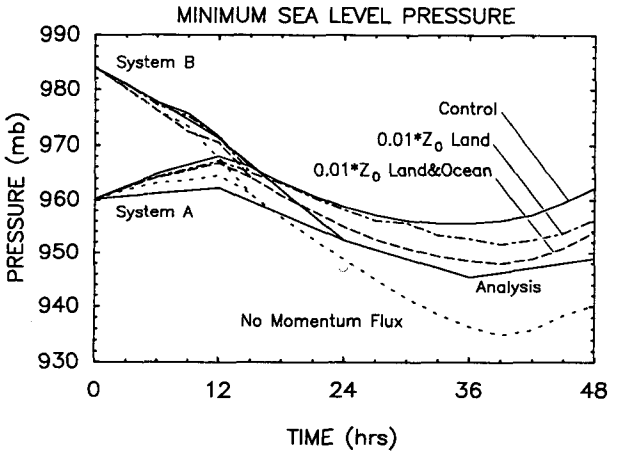

FIG. 14. Time evolution of minimum sea level pressure of systems A and B derived from ECMWF data and four simulations. For system B, sea level pressure is taken at point of maximum vorticity in lowest model sigma layer (i.e., lowest 80 m).

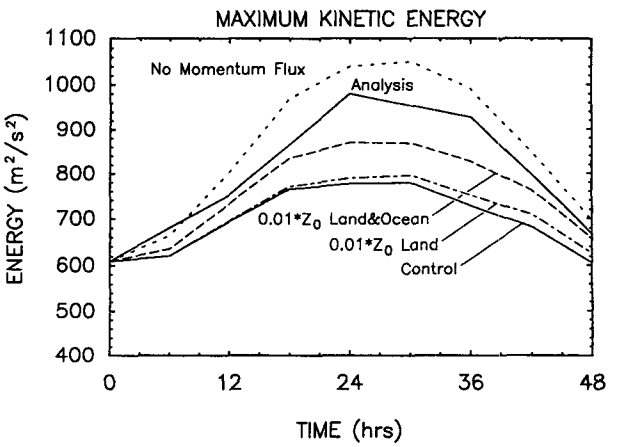

FIG. 15. Temporal evolution of maximum vertically averaged kinetic energy from ECMWF data (Analysis, upper solid line) and four simulations: Control (lower solid line), No Momentum Flux (dotted), $0.01*z_{0,\text{land and ocean}}$ (dashed), and $0.01*z_{0,\text{land}}$ (dash-dot).

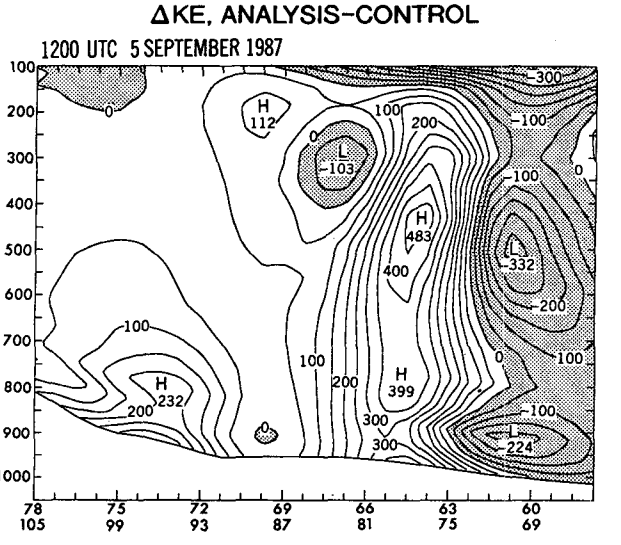

FIG. 16. Cross section at BB′ (see Fig. 7b) of the difference in kinetic energy between the analysis (ECMWF) and the Control simulation at 1200 UTC 5 September (24 h). Contour interval: 50 $m^2 s^{-2}$, negative values are shaded, abscissa as in Fig. 8.

when z_0 is reduced or drag is eliminated. Figure 17a shows a cross section of the Control kinetic energy, and Figs. 17b,c,d show the difference from the Control for the $0.01*z_{0,\text{land}}$ case, the NMF case, and the $0.01*z_{0,\text{land and ocean}}$ case, respectively. The results for the NMF and the $0.01*z_{0,\text{land and ocean}}$ case are qualitatively similar, with a large increase of kinetic energy at the surface (as expected based on surface drag considerations) and a rather uniform increase over the entire column up to the level of the jet. There are a number of different processes that might be responsible for the increase above the boundary layer. First, the increase in the low-level winds would tend to make the whole jet more barotropic, with reduced vertical advection of kinetic energy because of smaller vertical gradients of kinetic energy, reduced vertical velocities at lower levels (as was seen in Fig. 14c), or both. Kinetic energy levels can also vary due to local changes in the intensity of horizontal advection of geopotential height, $(\mathbf{V}\cdot\nabla\Phi)$, which can act as a source/sink of kinetic energy. This term is related to $\omega\alpha$ (α is the inverse of density), which affects the generation of kinetic energy throughout the entire column. Similar tendencies in baroclinic development with and without drag were found by Valdes and Hoskins (1988).

Clearly, the simulation of this storm was improved when z_0 was reduced from the default model values. The sea level pressure, the vertically averaged kinetic energy, and the vertical distribution of kinetic energy were all closer to the analysis. The boundary-layer parameterization used in the model is the so-called "E2 physics" (Miyakoda and Sirutis 1977), which uses Monin–Obukhov similarity theory in the constant flux layer. This parameterization depends crucially on the

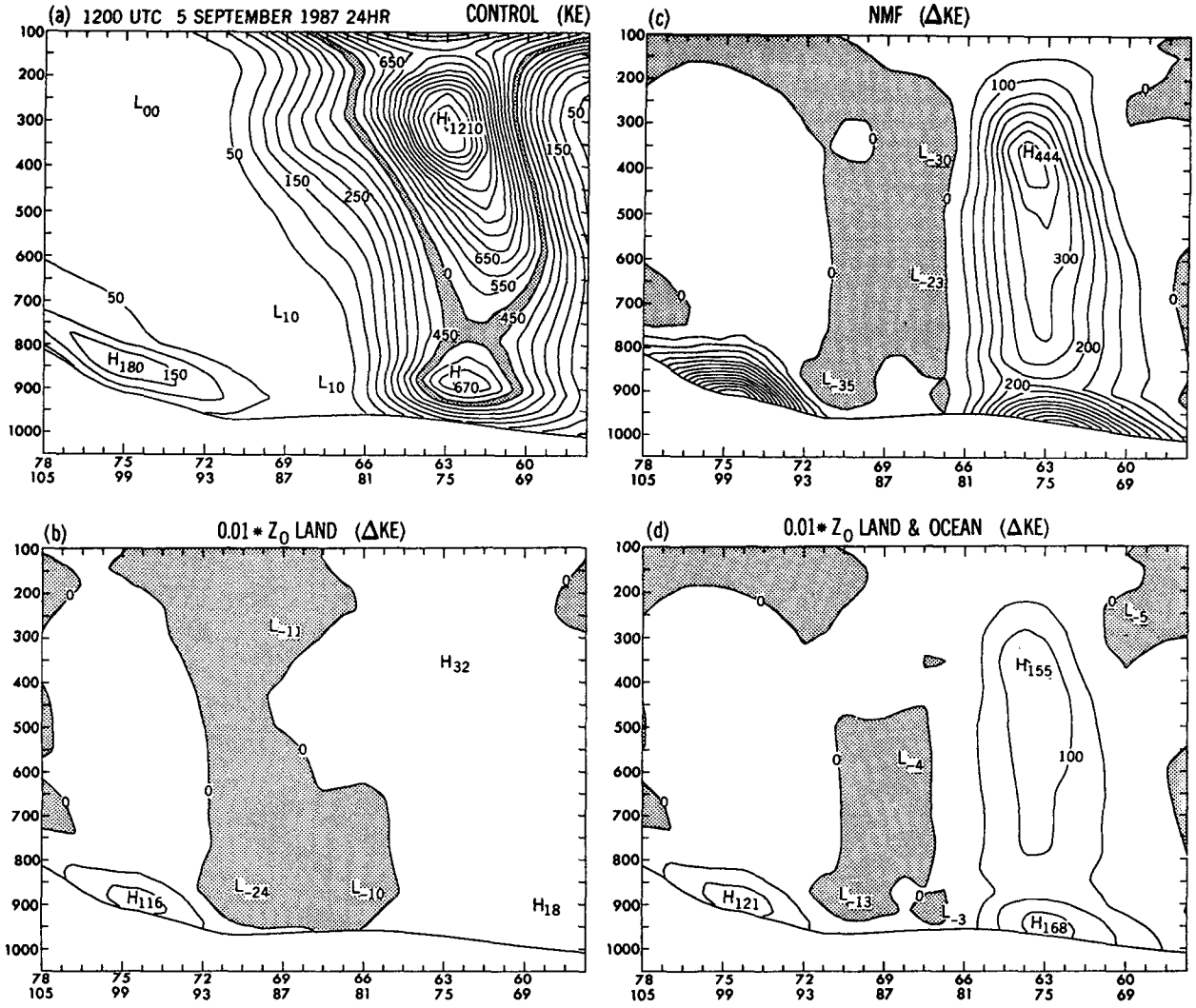

FIG. 17. Cross sections at BB′ (see Fig. 7b) of kinetic energy (contour interval: 50 $m^2 s^{-2}$) at 1200 UTC 5 September (24 h into simulation): (a) Control KE (shaded between 450 and 500 $m^2 s^{-2}$); (b), (c), and (d) are KE difference from Control for the $0.01*z_{0,\text{land}}$ case, the NMF case, and the $0.01*z_{0,\text{land and ocean}}$ case, respectively (negative differences shaded). Abscissa as in Fig. 8.

stability of the surface layer of the atmosphere as well as the ocean and land roughness height. Allowing for the possibility that the lack of data over the South Pacific may have affected the "analysis" used in this case, the sensitivity studies performed here imply a need to reduce the roughness heights not only over sea ice (which defaults to $z_{0,\text{land}}$), but over the ocean as well. The factor of 100 used in these experiments seems large, but the model only "feels" the drag from the constant flux layer, $\tau = \rho C_d |\mathbf{V}| \mathbf{V}$, and C_d, which is approximately proportional to $\ln(z_0)$, only changes by a factor of two with such a change in z_0. The Charnock (1955) formulation is used to calculate z_0 over the ocean and, given the stability characteristics of the constant flux layer, C_d can be calculated using Monin–Obukhov similarity theory. The calculated values of C_d in the vicinity of the storm were 1.7×10^{-3} for the Control simulation, and 0.77×10^{-3} for the $0.01 * z_{0,\text{land and ocean}}$ case. These values are within the range of possible values found by Smith (1988) who reviewed the values of the drag coefficient over ocean surfaces for extratropical oceanic conditions in winter under various atmospheric stability conditions.

Most global models used for operational forecasts by the world meteorological centers employ boundary-layer parameterizations similar to that used here, with z_0 values similar to those used in the Control case. The poor forecast skill of these models in the Southern Hemisphere extratropics has traditionally been attributed primarily to a lack of data. However, it has been reported that many low-resolution climate models also have difficulty reproducing the observed low zonal-average surface pressures near 60°S (Xu and von Storch 1990). The results of the current study suggest that a reduction in ocean roughness height for these models in areas of strong winds could remedy this deficiency by producing more intense cyclone systems with lower sea level pressure. The poleward migration of midlatitude systems would then produce the ensemble effect of reducing the zonal average sea level pressure in the subpolar region. At first glance, this approach would seem to exacerbate another problem with these models because they already tend to produce wintertime polar jets that are both too strong and too zonal, implying that an *increase* of surface drag is required in order to reduce the speed of the jet. However, while the models' surface drag and heat fluxes in the calm, statically stable tropical regions may indeed be too small (Smith 1988), the drag in areas of strong winds in the subpolar regions is probably already sufficiently high. A decrease in the surface drag in this region could, by producing stronger cyclones, also promote a more efficient interaction between the cyclones and the planetary flow, reducing the excessive speed and zonality of the polar jet. Although the variations of z_0 and C_d used here do not drastically affect the overall quality of the simulation(s) of this particular cyclone, there remain sufficient discrepancies regarding this issue to warrant further research.

5. Summary and conclusions

On 5 September 1987, an explosive storm occurred near 90°W in the South Pacific Ocean in a region that is known climatologically to be very cyclogenetic. The storm structure and the effects of topographic forcings and surface fluxes on the development of this storm were analyzed using model simulations.

The cyclone, developed as a disturbance in the subtropics, was drawn into a wave in the polar westerlies. As the storm intensified, the subtropical jet was deflected poleward and merged with the polar jet, transporting warm, moist subtropical air to sub-Antarctic regions. This deepening produced strong poleward winds within the warm air at all levels. The system finally occluded near the Antarctic continent. Small vertical wind shears and vertical tilt with height of the frontal system indicated a significant barotropic component.

Through the use of Lagrangian trajectories, the region of warm, moist ascent along the frontal zone was delineated, and the bifurcation of the flow as it neared the Antarctic continent was identified. The air that originated in the lower troposphere equatorward of the storm center was lifted as it moved poleward and curved either cyclonically around the upper-level low or anticyclonically as it flowed into the downstream ridge. Trajectories also showed that air circulated completely around the cyclone in lower levels, rising on the eastern side and sinking on the western side.

The roles of orography and surface forcing were investigated through sensitivity studies. It was found that the development of this storm was not strongly influenced by orography or surface heat fluxes, although the upper-level jet was slightly stronger without topography. The surface heat fluxes were found to be weak in the early development of the storm, although they may have been important in creating a more unstable environment prior to development. Only at later stages of development were the surface heat fluxes significant, primarily in the cold air behind the front.

The decrease in the surface roughness parameter over land and sea was found to significantly increase the intensity of the storm, producing a lower sea level pressure minimum and a stronger kinetic energy maximum. The swiftness with which the entire troposphere responds to the change in surface roughness, as measured by the rapid change in the vertically averaged kinetic energy, suggests that surface processes could be directly linked with the upper-level jet in the area of maximum ascent. These results suggest that the default values of z_0 (on the order of 0.1 cm) and C_d (on the order of 1.7×10^{-3}) over the ocean surface are probably too high. A more realistic value for C_d would probably be on the order of 0.7×10^{-3}. This reduced value of surface drag over the high-latitude oceans in areas of strong winds should result in the production of more intense marine cyclone development with deeper sea level pressures than those predicted by the present operational models. The sensitivity studies performed

here have shown that neither topography nor surface forcing played a major role in the development of this storm. One plausible explanation for cyclogenesis in this case seems to be a combination of internal baroclinic and barotropic processes. It was found through analysis of the sector-averaged PV prior to the development that the necessary condition for barotropic and/or baroclinic instability was satisfied in the region between the subtropical and polar jets. The environment appeared to be unstable enough to allow the wave to develop without surface or orographic forcings. Our analysis suggests that the strong development to an intense mature cyclone was a product of the unique configuration of the dual jet structure in the South Pacific. Initially, the wave intensified concurrently in both branches of the westerlies due to either baroclinic or barotropic processes. As the wave system developed, the two jets merged. The extended trough resulting from this merger produced strong poleward heat transport, contributing to subsequent strong baroclinic development. In this analysis, it was not possible to separate the relative contribution of barotropic and baroclinic processes in the development of the wave. This topic is currently being investigated, and the results will be published elsewhere.[2]

Acknowledgments. The authors wish to extend their deepest appreciation to Mr. John Sheldon, who ran the additional simulations which were used in the revised version of the paper, and to Larry Polinsky, who computed the 30-day mean statistics. The authors also appreciate the comments of Mr. Sheldon, Bill Stern, and Bob Tuleya, which helped improve the paper. The ECMWF analysis was kindly provided by Dr. G. Sommeria. The data for the time mean was prepared by Dr. N.-C. Lau and Alexis Lau. The authors wish to thank Phil Tunison and the GFDL drafting department, and photographer John Conner for the preparation of the figures. Acknowledgment is extended to the computer center of the Argentine Atomic Energy Commission for the use of its facilities.

[2] *Note added in proof.* During the review period of this paper, a companion paper on the storm energetics was published by the lead authors earlier in this volume.

REFERENCES

Bosart, L., and S. C. Lin, 1984: A diagnostic analysis of the Presidents' Day Storm of February 1979. *Mon. Wea. Rev.*, **112,** 2148–2177.

Carleton, A. M., 1979: A synoptic climatology of satellite-observed extratropical cyclone activity for the Southern Hemisphere winter. *Arch. Meteor. Geophys. Bioklim. Ser. B.* **27,** 265.

——, 1981: Monthly variability of satellite derived cyclonic activity for the Southern Hemisphere winter. *J. Climatol.* **1,** 21–38.

Charney, J. G., and M. E. Stern, 1962: On the stability of internal baroclinic jets in a rotating atmosphere. *J. Atmos. Sci.*, **19,** 159–172.

Charnock, H., 1955: Wind stress on a water surface. *Quart. J. Roy. Meteor. Soc.*, **81,** 639–640.

Hoskins, B. J., and P. Berrisford, 1988: The storm of 15–16 October 1987: A potential vorticity perspective. *Weather,* **43,** 122–129.

——, M. E. McIntyre and A. W. Robertson, 1985: On the use and significance of isentropic potential vorticity maps. *Quart. J. Roy. Meteor. Soc.*, **116,** 525–560.

Karoly, D. J., and A. H. Oort, 1987: A comparison of Southern Hemisphere circulation statistics based on GFDL and Australian analyses. *Mon. Wea. Rev.*, **115,** 2033–2059.

Kuo, Y.-H., and S. Low-Nam, 1990: Prediction of nine explosive cyclones over the western Atlantic Ocean with a regional model. *Mon. Wea. Rev.*, **118,** 3–25.

McKenna, D. S., R. L. Jones, J. Austin, E. V. Browell, M. P. McCormick, A. J. Krueger and A. F. Tuck, 1989: Diagnostic studies of the Antarctic Vortex during the 1987 Airborne Antarctic Ozone Experiment: Ozone miniholes. *J. Geophys. Res.*, **94,** 11 641–11 668.

Miyakoda, K., and J. Sirutis, 1977: Comparative integrations of global models with various parameterizations: Processes of subgrid vertical transport. *Contrib. Atmos. Phys.*, **50,** 445–487.

Oort, A. H., 1983: Global atmosphere circulation statistics, 1958–1973. NOAA Professional Pap. No. 14, U.S. Govt. Printing Office, Washington, D.C.

Orlanski, I., and J. J. Katzfey, 1987: Sensitivity of model simulations for a coastal cyclone. *Mon. Wea. Rev.*, **115,** 2792–2821.

——, B. B. Ross, L. J. Polinsky and R. W. Shaginaw, 1985: Advances in the theory of atmospheric fronts. *Adv. Geophys.*, **28B,** 223–252.

——, J. J. Katzfey, M. Marino and C. Menendez, 1989: The role of cyclones in the daily variability of Antarctic ozone. *J. Proc. Third Int. Conf. on Southern Hemisphere. Meteorology and Oceanography,* Amer. Meteor. Soc., p. 441.

Pettersen, S., and S. Smebye, 1971: On the development of extratropical storms. *Quart. J. Roy. Meteor. Soc.*, **97,** 457–482.

Physick, W. L., 1981: Winter depression tracks and climatological jet streams in the Southern Hemisphere during FGGE year. *Quart. J. Roy. Meteor. Soc.*, **107,** 883–898.

Randel, W. J., 1988: The seasonal evolution of planetary waves in the Southern Hemisphere stratosphere and troposphere. *Quart. J. Roy. Meteor. Soc.*, **114,** 1385–1409.

Reed, R. J., 1979: Cyclogenesis in polar air streams. *Mon. Wea. Rev.*, **107,** 38–52.

——, and M. D. Albright, 1986: A case study of explosive cyclogenesis in the eastern Pacific. *Mon. Wea. Rev.*, **114,** 2297–2319.

Shapiro, M., 1980: Turbulent mixing within tropopause folds as mechanisms for the exchange of chemical constituents between the stratosphere and troposphere. *J. Atmos. Sci.*, **37,** 994–1004.

Smith, S., 1988: Coefficients for sea surface wind stress, heat flux, and wind profiles as a function of wind speed and temperature. *J. Geophys. Rev.*, **93,** 15 467–15 472.

Streten, N. A., 1980: Some synoptic indices of the Southern Hemisphere mean sea level circulation 1972–1977. *Mon. Wea. Rev.*, **108,** 18–36.

——, and A. J. Troup, 1973: A synoptic climatology of satellite-observed cloud vortices over the Southern Hemisphere. *Quart. J. Roy. Meteor. Soc.*, **99,** 56–72.

Trenberth, K. E., 1981: Observed Southern Hemisphere eddy statistics at 500 mb: Frequency and spatial dependence. *J. Atmos. Sci.*, **38,** 2585–2605.

——, 1986: An assessment of the impact of transient eddies on the zonal flow during blocking episode using localized Eliassen–Palm flux diagnostics. *J. Atmos. Sci.*, **43,** 2070–2087.

Uccellini, L. W., D. Keyser, K. F. Brill and C. H. Wash, 1985: The Presidents' Day Cyclone of 18–19 February 1979: Influence of upstream trough amplification and associated tropopause folding on rapid cyclogenesis. *Mon. Wea. Rev.*, **113,** 962–987.

Valdes, P. J., and B. J. Hoskins, 1988: Baroclinic instability of the zonally averaged flow with boundary layer damping. *J. Atmos. Sci.*, **45,** 1584–1593.

van Loon, H., and R. L. Jenne, 1972: The zonal harmonic standing waves in the Southern Hemisphere. *J. Geophys. Res.*, **77,** 992–1003.

Xu, J., and H. von Storch, 1990: The performance of four spectral GCM's in the Southern Hemisphere: The January and July climatology and the semiannual wave. *J. Climate,* **3,** 53–69.